JOURNAL OF PROPULSION AND POWER
Vol. 26, No. 5, September–October 2010

# Numerical Simulation of Gaseous Hydrocarbon Fuel Injection in a Hypersonic Inlet

Yen-W. Wang* and Jean P. Sislian†
*University of Toronto, Toronto, Ontario M3H 5T6, Canada*

DOI: 10.2514/1.47741

**The performance of gaseous hydrocarbon/air mixing in the inlet of a scramjet is investigated in this paper. The two-oblique-shock mixed-compression inlet configuration is selected, and cantilevered ramp injectors, designed to deliver rapid mixing in a high-enthalpy flow, are placed strategically near the leading edge of the inlet. Air inflow conditions correspond to a Mach 8 flight at a dynamic pressure of 67,032 Pa at a 28.6 km altitude. The objective of this study is to evaluate the impact of inlet geometrical parameters, fuel-injection properties, and injector dimensions on the mixing efficiency. Both light ($CH_4$) and heavy ($C_{12}H_{24}$) hydrocarbon fuels are considered. The analysis of three-dimensional steady-state flowfields is undertaken numerically, using the WARP code. WARP solves the multispecies Favre-averaged Navier–Stokes equations, which are closed by the Wilcox $k$-$\omega$ turbulence model. The numerical results indicate that a mixing efficiency of up to 95.8% can be achieved with a low risk of premature ignition. Inlet compression ratio, fuel-tank stagnation temperature, and fuel/air equivalence ratio are all identified as having a significant influence on inlet fuel-injection performance. The applicability of the cantilevered ramp injector to the Mach 8 hydrocarbon inlet is validated and justified.**

## Nomenclature

| | | |
|---|---|---|
| $c$ | = | mass fraction of the species |
| $d_w$ | = | distance from wall to first inner node |
| $\mathcal{F}_{\text{pot}}$ | = | thrust potential |
| $\mathcal{F}_{\text{pot,ref}}$ | = | reference thrust potential at the engine inlet |
| $\mathcal{H}_{\text{duct}}$ | = | height of the internal mixing duct |
| $\mathcal{H}_{\text{inj}}$ | = | height of the fuel-injection area |
| $\mathcal{H}_{\text{inl}}$ | = | height of the inlet |
| $k$ | = | turbulence kinetic energy |
| $\mathcal{L}_{\text{cowl}}$ | = | length of the external mixing region |
| $\mathcal{L}_{\text{inj}}$ | = | length of the injector |
| $\mathcal{L}_{\text{inl}}$ | = | length of the inlet |
| $\mathcal{L}_{\text{ramp}}$ | = | distance from the inlet leading edge to the fuel injector |
| $M$ | = | Mach number |
| $\dot{m}$ | = | mass flow rate |
| $\dot{m}_{\text{air,inlet}}$ | = | mass flow rate of the inlet captured air |
| $P$ | = | pressure |
| $P^\star$ | = | effective pressure, $P + 2/3\rho k$ |
| $Pr_T$ | = | turbulence Prandtl number |
| $q$ | = | flight dynamic pressure |
| $r$ | = | grid density factor |
| $Sc_T$ | = | turbulence Schmidt number |
| $T$ | = | temperature |
| $U$ | = | magnitude of the velocity vector |
| $\mathcal{W}_{\text{array}}$ | = | width of the injector array |
| $\mathcal{W}_{\text{inj}}$ | = | width of the fuel-injection area |
| $X, Y, Z$ | = | Cartesian coordinates |
| $\eta_m$ | = | mixing efficiency |
| $\theta_{c1}$ | = | compression angle of injector 1 |
| $\theta_{c2}$ | = | compression angle of injector 2 |
| $\theta_e$ | = | expansion angle of the injector |
| $\theta_{\text{inl}}$ | = | inlet leading-wedge angle |
| $\theta_s$ | = | sweep angle of the injector |
| $\mu$ | = | viscosity |
| $\rho$ | = | density |
| $\phi$ | = | global equivalence ratio |
| $\omega$ | = | dissipation rate per unit of turbulence kinetic energy |

*Subscripts*

| | | |
|---|---|---|
| avg | = | averaged |
| $b$ | = | plane of interest |
| $c$ | = | plane of interest reversibly expanded to constant pressure at the vehicle exit area |
| $f$ | = | fuel stream |
| 0 | = | freestream |

*Superscripts*

| | | |
|---|---|---|
| $R$ | = | reacting |
| $S$ | = | stoichiometric |
| $\circ$ | = | stagnation |

Presented as Paper 2008-2533 at the 15th AIAA International Space Planes and Hypersonic Systems and Technologies Conference, Dayton, OH, 28 April–1 May 2008; received 15 November 2009; revision received 16 March 2010; accepted for publication 16 March 2010. 

*Graduate Student, Institute for Aerospace Studies, High-Speed Vehicle Propulsion Systems Group, 4925 Dufferin Street; yen.wang@utoronto.ca. Student Member AIAA.

†Professor, Institute for Aerospace Studies, High-Speed Vehicle Propulsion Systems Group, 4925 Dufferin Street; sislian@caius.utias.utoronto.ca. Associate Fellow AIAA.

## I. Introduction

THE concept of fuel injection in the inlet of a hypersonic engine has lately attracted the attention of researchers [1–3]. This technique can prove to be advantageous in the range of the very high-flight Mach numbers, where the residence time of diffusively burning flows becomes excessively long in the combustor of an engine. By relocating the fuel injectors from their traditional combustor positions to the leading edge of the inlet, fuel/air mixing processes can be organized in the long inlet forebody, which is typical of most hypersonic vehicles. This modification may result in increased fuel/air mixing efficiency and also has the potential to appreciably shorten the length of the combustion chamber. However, the feasibility of this concept hinges on the formidable task of avoiding premature ignition of the resulting combustible mixture in the boundary layers of the inlet and flashback. Some success in achieving these goals has been reported in the previously cited references.

Recently, the concept of fuel injection in the inlet of the engine has regained impetus due to recent efforts of developing scramjet engines using hydrocarbon fuels in the flight Mach number range of 4–8. It is

argued that, due to the multistage physical–chemical processes of the liquid fuel breaking up into droplets, their subsequent vaporization and ignition delay times, and the short residence time available in the combustor, the conventional fuel-injection techniques may not be effective for hydrocarbon fuels [3]. Injecting part or all of the fuel in the inlet or isolator of the engine can prove to be beneficial in enhancing the fuel/air mixing process, hence shortening the combustor length.

The injection of the liquid and gaseous hydrocarbon fuels in the inlet or isolator of a scramjet has been experimentally and numerically investigated [4–8]. In these references, hydrocarbon fuels are injected normally through wall orifices that are located behind and in the vicinity of the flat blunt trailing edge of a sharp triangular pylon. This configuration aims to increase the penetration height and spreading rate of the fuel into the oncoming supersonic inlet flow. In the experimental works performed by Vinogradov and Prudnikov [4], Livingston et al. [5], and Owens et al. [6], liquid kerosene fuel is injected into $M = 1.6$–$4.0$ airflows behind sharp triangular pylons under various stagnation conditions and low-fuel/air equivalence ratios. The presented shadowgraph and schlieren images of the resulting fuel/air mixtures in the inlet do indeed show that high fuel penetration is achieved and, for relatively low fuel pressures, the liquid fuel is removed away from the wall when compared with the case of when the pylons are absent. A shadowgraph image of a combusting case also shows that combustion is confined to the test section with no noticeable upstream effects. Losses due to the liquid kerosene injection and mixing are quantified by measured total pressure losses. It is concluded that liquid kerosene injection in the isolator of the inlet at $M = 1.6$, with equivalence ratios less than 0.5, does not result in any airflow choking and has no substantial effect on the isolator shock train [6]. In addition to liquid kerosene, Vinogradov et al. [7] also investigated the gaseous methane fuel at equivalence ratios of up to 0.85 and total fuel temperatures of 550–880 K. In their experiments, gaseous methane was normally injected behind a series of triangular and swept pylons, which were placed on the upper and lower walls of an inlet-isolator duct, and an oncoming $M = 2$ airflow under various stagnation pressures (0.4–0.7 MPa) and stagnation temperature (650–910 K) conditions. Analysis of the experimental data on heat flux and the distributions of combustion efficiency along the isolator-combustor duct indicates the absence of combustion in the isolator.

In a more relevant study to the one presented herein, Guoskov et al. [8] conducted a numerical investigation of gaseous hydrocarbon fuel (ethylene and propane) injection in the wake of the thin-swept triangular pylons placed normally to the sidewalls of a sidewall compression inlet, which consisted of two opposed swept wedge walls, at both $M = 6$ and 8. The analysis of the flowfield generated by the sonic, normal wall fuel injection behind an individual pylon is performed by using the full Favre-averaged Navier–Stokes equations for the three-dimensional turbulent, multispecies, and nonreacting flows and closed with a differential one-parameter turbulence model. Parabolized Navier–Stokes equations are employed to calculate the flowfield downstream of the pylons when the normally injected fuel turns parallel to the mainstream and becomes supersonic, by assuming that individual jets from different pylons do not interact with one another and the wall boundaries. For fuel/air equivalence ratios of 0.3–0.7, fuel/air mixing efficiencies between 0.95 and 0.98 are reported within an inlet channel length of 0.65 m. However, it should be noted that, as the authors of the study state, the adopted computational technique is quite approximate. A comprehensive and more complete review of this round of investigations is summarized by Vinogradov et al. [3].

The present paper is likewise concerned with the numerical simulations of the flowfield generated by gaseous hydrocarbon fuel being injected into the inlet of a hypersonic vehicle. However, unlike the investigation performed by Guoskov et al. [8], the fuel is injected quasi parallel to the compression surface of the inlet, where the cantilevered ramp injectors are located. The objective of the investigation is to assess the impact of the inlet compression, the fuel-injection conditions, fuel selection and properties, and injector geometry on the overall fuel/air mixing efficiency and the attendant flow losses at the exit of the inlet. The possibility of premature ignition of the resulting combustible mixture in the inlet or in its wall boundary layers is also assessed via a finite-rate chemical kinetics model. A detailed description of the considered inlets, fuel types, injection conditions, and injector configurations is given in the next paragraph. This is followed by a brief presentation of the flow-governing equations and their numerical solution technique, together with the imposed boundary conditions. Global performance parameters (mixing efficiency and thrust potential) are introduced, and a grid convergence study is performed to assess the accuracy of the predictions. A detailed discussion of the obtained results are considered next. The effects of the inlet configurations and compression, fuel injector geometry, fuel type, and fuel-injection conditions, as well as of the fuel/air equivalence ratio, on the general flowfield behavior and global performance parameters are discussed in detail. The paper concludes with a final paragraph summarizing the main findings of the presented study.

## II. Inlet and Fuel Injector Configurations

Generic two- and three-shock mixed-compression-type inlets, as illustrated in Fig. 1, at a flight Mach number of $M_0 = 8$ and a flight dynamic pressure of $q = 67,032$ Pa (1400 psf) are considered in the present study, resulting in an air inflow pressure of $P_0 = 1.50$ KPa, a temperature of $T_0 = 225$ K, and a velocity of $U_0 = 2410$ m/s at an altitude of 28.5 km. In all cases, the inlet is assumed to operate at ondesign conditions (i.e., the shock emanating from its leading edge terminates on the cowl tip, where the internal second shock is formed). The strength of the shocks, the inlet flowfield parameters, the compression ratio, and its exit-to-inflow area ratio are determined from two requirements:

1) Due to the configuration and geometry of the employed inlet, the inlet exit flow must be parallel to the flight direction.

2) The temperature of the combustible mixture after the last shock is fixed and prescribed at $T = 750$–$1300$ K, depending on the ignition characteristics of the injected fuel, to avoid premature ignition of the mixture in the inlet.

In the three-shock inlet case, the first two shocks are assumed to be of equal strengths (i.e., have equal pressure ratios across them). Because of fuel injection, the inlet flowfield and its dimensions [i.e., the length of the external mixing region $\mathcal{L}_{\text{cowl}}$ (Fig. 1), its height $\mathcal{H}_{\text{inl}}$, the height of its internal mixing duct $\mathcal{H}_{\text{duct}}$, and its overall length $\mathcal{L}_{\text{inl}}$] all depend on the amount of injected fuel and its mixing efficiency

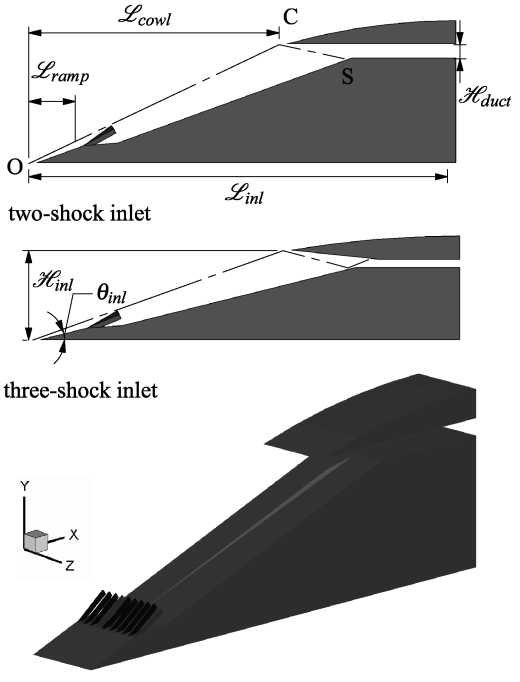


**Fig. 1 Inlet configuration.**

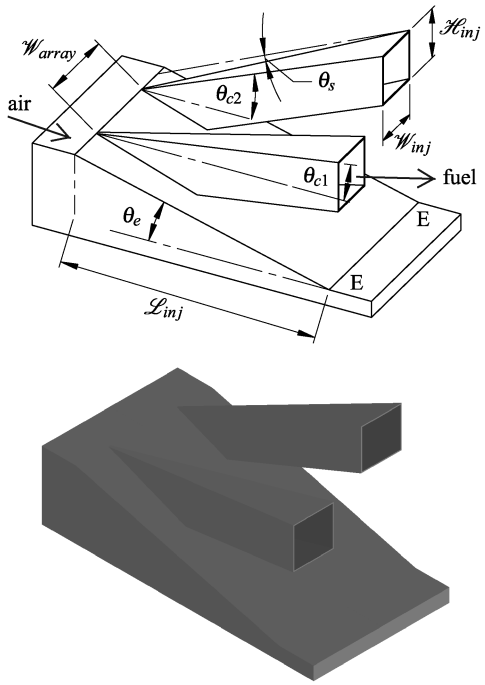


**Fig. 2 Cantilevered ramp fuel injector.**

with incoming air. Therefore, they can only be determined interactively, a posteriori, via numerical simulation.

Fuel is injected quasi parallel to the compression surface of the inlet via a cantilevered ramp injector, which has shown to successfully keep the fuel away from the inlet boundary layers [9,10]. A previously investigated geometry of such an injector [1] exhibiting high-fuel/air mixing efficiency and minimal losses, as depicted in Fig. 2, is positioned on the inlet wall at a fixed distance $\mathcal{L}_{\text{ramp}} = 0.2$ m from its leading edge. Unless otherwise specified, the injector protrudes into the airflow with alternating 9/16° compression angles ($\theta_{c1}/\theta_{c2}$), and both of its sidewalls have a (negative) sweep angle $\theta_s = -0.8°$. Its expansion angle $\theta_e$ varies from 7 to 15°, depending on the magnitude of the inlet leading-wedge angle $\theta_{\text{inl}}$. Its dimensions are held constant for all cases unless otherwise specified. The fuel-injection area is 20 mm($\mathcal{H}_{\text{inj}}$) × 5 mm($\mathcal{W}_{\text{inj}}$), the spacing between the injectors is 20 mm ($\mathcal{W}_{\text{array}}$), and the overall injector length is 150 mm ($\mathcal{L}_{\text{inj}}$). To assess the impact of the molecular weight of gaseous hydrocarbon fuels on their mixing characteristics with the inlet airflow, a light fuel methane ($CH_4$) and a heavy fuel kerosene ($C_{12}H_{24}$), with widely differing specific weights, are considered.

The effects of four quantities are investigated by varying only one quantity, while others are held constant: the degree of inlet compression as characterized by the angle $\theta_{\text{inl}}$, the stagnation temperature of the injected fuel $T_f^\circ$, the global equivalence ratio of the fuel/air mixture $\phi$, and the molecular weight of the fuel. An attempt has also been made to optimize the mixing efficiency of the cantilevered ramp injector by varying its geometrical parameters. All the investigated cases are summarized in Tables 1–4 and grouped according to the quantity being modified.

## III. Numerical Technique

Since the governing equations employed in the present study and their numerical solution techniques are presented in detail elsewhere [2,11,12], they are briefly discussed here for completeness. The three-dimensional hypersonic, turbulent, multispecies flowfield resulting from the fuel/air mixing process in the inlet is described by Favre-averaged Navier–Stokes equations, closed by the Wilcox $k$-$\omega$ turbulence model [13]. Unless otherwise specified, the turbulence Schmidt and Prandtl numbers are set to $Sc_T = 1.0$ and $Pr_T = 0.9$. A finite-rate methane/air chemical reaction model is used to assess the possibility of premature ignition in the combustible mixture before the combustor of the engine (see Sec. IV.D). The system of equations is discretized using centered second-order finite differences for all the derivatives except the convection term, which is discretized using the approximate Riemann solver of Roe [14] and made second-order accurate through a symmetric minmod limiter by Yee et al. [15]. The discretized residual is solved to steady state by a block-implicit factorization algorithm [16], chosen for its ability to solve the Roe scheme without the need for introducing an explicit artificial dissipation term in the residual (the entropy correction term) to stabilize the iterative process. Since this term can lead to excessive dissipation in shear layers, it is not included in the simulations reported herein. The convergence criterion is based on the magnitude of both continuity and energy residuals. The discretization technique is implemented in the WARP code, which is used extensively for the numerical solution of the flowfields considered in the present study. Details and capabilities of the WARP code are given in the previously cited references.

### A. Boundary Conditions

The inlet is assumed to be constituted by an infinite number of spanwise arrays that are located sufficiently far away from the sidewalls of the inlet. The characteristics of the flowfield are investigated by concentrating on only one array, for which the lateral $Z$-direction boundaries, $Z = 0$ and $Z = \mathcal{W}_{\text{array}}$, coincide with the midplanes of the $\theta_{c1}$ and $\theta_{c2}$ fuel injectors, shown in Fig. 2. A representative array is illustrated as the light-gray section in Fig. 1. Second-order-accurate symmetry conditions are imposed on the $Z = 0$ and $Z = \mathcal{W}_{\text{array}}$ planes to obtain $P^\star$, $\rho$, $k$, $\omega$, and the velocity component tangent to the symmetry planes, while the perpendicular velocity component is set to zero. At the walls, the velocity and turbulence kinetic energy are fixed to zero, and the turbulence dissipation rate is specified as $\omega = 36\mu/5\rho d_w^2$, $d_w$ being the distance between the near-wall node and the wall ($d_w = 10$–$30$ $\mu$m). A short 5-mm-long runway is imposed on the fuel jet before injection to avoid a singularity in the turbulence and other flow properties at the start of the mixing layer; this also reduces the solution sensitivity to the freestream value of $\omega$. The external and internal inlet duct walls and the injector surfaces are all assumed to be no-slip and fuel-cooled to a plausible estimated constant temperature of 500 K. The upstream boundary of the inlet is specified to have the supersonic inflow

**Table 1 Case summary: Effect of inlet compression $\theta_{\text{inl}}$**

| | | | Mass-averaged flow variables after last shock | | | Fuel-injection system properties | | | | | Inlet dimensions | | | Performance parameters | |
|---|---|---|---|---|---|---|---|---|---|---|---|---|---|---|---|
| Case | Fuel | $\theta_{\text{inl}}$, deg | $P_{\text{avg}}/P_0$ | $T_{\text{avg}}/T_0$ | $U_{\text{avg}}$, m/s | $\phi$ | $T_f^\circ$, K | $P_f^\circ$, MPa | $T_f$, K | $U_f$, m/s | $\mathcal{L}_{\text{cowl}}$, m | $\mathcal{H}_{\text{inl}}$, mm | $\mathcal{H}_{\text{duct}}$, mm | $\mathcal{F}_{\text{pot}}$, Ns/kg | $\eta_m$, % |
| 1 | $CH_4$ | 16.4 | 47.13 | 4.31 | 1926 | 1.05 | 1400 | 28.92 | 221 | 2228 | 1.122 | 452 | 59.5 | −2.5 | 63.5 |
| 2 | $CH_4$ | 20.7 | 74.80 | 5.32 | 1718 | 1.06 | 1400 | 21.38 | 276 | 2213 | 1.076 | 513 | 59.7 | −65.4 | 73.7 |
| 3 | $CH_4$ | 16.4 | 45.73 | 4.27 | 1883 | 1.09 | 800 | 8.616 | 160 | 1610 | 1.076 | 433 | 59.7 | −39.1 | 56.8 |
| 4 | $CH_4$ | 20.7 | 76.22 | 5.33 | 1661 | 1.09 | 800 | 6.199 | 200 | 1583 | 1.038 | 494 | 58.9 | −107.9 | 67.8 |
| Two- and three-shock inlets | | | | | | | | | | | | | | | |
| 5 | $CH_4$ | 20.7 | 78.34 | 5.36 | 1681 | 1.09 | 1100 | 12.57 | 236 | 1914 | 1.061 | 505 | 58.1 | −83.4 | 71.4 |
| 6 | $CH_4$ | 13.7 | 101.21 | 5.36 | 1641 | 1.00 | 1100 | 21.54 | 164 | 1953 | 1.181 | 414 | 38.9 | −117.2 | 75.5 |

**Table 2 Case summary: Effect of stagnation temperature of injected fuel $T_f^\circ$**

| | | | Mass-averaged flow variables after last shock | | | Fuel-injection system properties | | | | | Inlet dimensions | | | Performance parameters | |
|---|---|---|---|---|---|---|---|---|---|---|---|---|---|---|---|
| Case | Fuel | $\theta_{\text{inl}}$, deg | $P_{\text{avg}}/P_0$ | $T_{\text{avg}}/T_0$ | $U_{\text{avg}}$, m/s | $\phi$ | $T_f^\circ$, K | $P_f^\circ$, MPa | $T_f$, K | $U_f$, m/s | $\mathcal{L}_{\text{cowl}}$, m | $\mathcal{H}_{\text{inl}}$, mm | $\mathcal{H}_{\text{duct}}$, mm | $\mathcal{F}_{\text{pot}}$, Ns/kg | $\eta_m$, % |
| 3 | $CH_4$ | 16.4 | 45.73 | 4.27 | 1883 | 1.09 | 800 | 8.616 | 160 | 1610 | 1.076 | 433 | 59.7 | −39.1 | 56.8 |
| 1 | $CH_4$ | 16.4 | 47.13 | 4.31 | 1926 | 1.05 | 1400 | 28.92 | 221 | 2228 | 1.122 | 452 | 59.5 | −2.5 | 63.5 |
| 7 | $CH_4$ | 20.7 | 73.38 | 5.11 | 1682 | 1.33 | 800 | 12.51 | 160 | 1610 | 1.060 | 507 | 60.5 | −70.8 | 57.0 |
| 8 | $CH_4$ | 20.7 | 74.90 | 5.17 | 1737 | 1.28 | 1400 | 42.01 | 221 | 2228 | 1.101 | 528 | 60.4 | −26.3 | 64.5 |
| 9 | $CH_4$ | 20.7 | 79.38 | 5.56 | 1636 | 0.85 | 700 | 1.980 | 236 | 1402 | 1.012 | 479 | 57.8 | −146.1 | 79.8 |
| 10 | $CH_4$ | 20.7 | 85.39 | 5.66 | 1643 | 0.84 | 1100 | 5.548 | 314 | 1886 | 1.035 | 490 | 56.7 | −128.2 | 86.4 |

**Table 3 Case summary: Effect of fuel/air equivalence ratio $\phi$**

| | | | Mass-averaged flow variables after last shock | | | Fuel-injection system properties | | | | | Inlet dimensions | | | Performance parameters | |
|---|---|---|---|---|---|---|---|---|---|---|---|---|---|---|---|
| Case | Fuel | $\theta_{\text{inl}}$, deg | $P_{\text{avg}}/P_0$ | $T_{\text{avg}}/T_0$ | $U_{\text{avg}}$, m/s | $\phi$ | $T_f^\circ$, K | $P_f^\circ$, MPa | $T_f$, K | $U_f$, m/s | $\mathcal{L}_{\text{cowl}}$, m | $\mathcal{H}_{\text{inl}}$, mm | $\mathcal{H}_{\text{duct}}$, mm | $\mathcal{F}_{\text{pot}}$, Ns/kg | $\eta_m$, % |
| 11 | $C_{12}H_{24}$ | 12.5 | 26.42 | 3.90 | 1977 | 0.84 | 800 | 23.53 | 710 | 758 | 1.084 | 365 | 69.3 | −52.8 | 59.5 |
| 12 | $C_{12}H_{24}$ | 12.5 | 26.67 | 3.96 | 1976 | 0.66 | 800 | 1.099 | 746 | 595 | 1.047 | 351 | 66.5 | −74.5 | 73.2 |
| 5 | $CH_4$ | 20.7 | 78.34 | 5.36 | 1681 | 1.09 | 1100 | 12.57 | 236 | 1914 | 1.061 | 505 | 58.1 | −83.4 | 71.4 |
| 10 | $CH_4$ | 20.7 | 85.39 | 5.66 | 1643 | 0.84 | 1100 | 5.548 | 314 | 1886 | 1.035 | 490 | 56.7 | −128.2 | 86.4 |
| 13 | $CH_4$ | 20.7 | 81.31 | 5.80 | 1649 | 0.60 | 1100 | 2.379 | 460 | 1877 | 1.012 | 477 | 56.4 | −153.8 | 95.8 |
| Effect of fuel molecular weight | | | | | | | | | | | | | | | |
| 4 | $CH_4$ | 20.7 | 76.22 | 5.33 | 1661 | 1.09 | 800 | 6.199 | 200 | 1583 | 1.038 | 494 | 58.9 | −107.9 | 67.8 |
| 14 | $C_{12}H_{24}$ | 20.7 | 69.83 | 5.72 | 1585 | 1.08 | 800 | 2.627 | 745 | 601 | 0.959 | 461 | 61.6 | −162.5 | 63.4 |

**Table 4 Case summary: Effect of injector geometry**

| | | Average flow variables at exit of inlet | | | Fuel-injector dimensions | | | | | | Inlet dimensions | | | Performance parameters | |
|---|---|---|---|---|---|---|---|---|---|---|---|---|---|---|---|
| Case | $\phi$ | $P_{\text{avg}}/P_0$ | $T_{\text{avg}}/T_0$ | $U_{\text{avg}}$, m/s | $\theta_s$, deg | $\theta_{c1}$, deg | $\theta_{c2}$, deg | $\mathcal{W}_{\text{array}}$, mm | $\mathcal{H}_{\text{inj}}$, mm | $\mathcal{W}_{\text{inj}}$, mm | $\mathcal{L}_{\text{cowl}}$, m | $\mathcal{H}_{\text{inl}}$, mm | $\mathcal{H}_{\text{duct}}$, mm | $\mathcal{F}_{\text{pot}}$, Ns/kg | $\eta_m$, % |
| 8 | 1.28 | 74.90 | 5.17 | 1737 | −0.8 | 9 | 16 | 20 | 20 | 5 | 1.101 | 528 | 60.4 | −26.3 | 64.5 |
| 15 | 1.19 | 74.05 | 5.21 | 1752 | 0.0 | 9 | 16 | 20 | 20 | 5 | 1.191 | 576 | 66.3 | −28.0 | 60.1 |
| 16 | 1.26 | 76.80 | 5.25 | 1732 | −0.8 | 12.5 | 12.5 | 20 | 20 | 5 | 1.127 | 542 | 61.2 | −28.9 | 49.2 |
| 17 | 1.57 | 80.89 | 5.18 | 1733 | −0.8 | 9 | 16 | 15 | 20 | 5 | 1.165 | 571 | 64.9 | 17.6 | 45.5 |
| 18 | 1.06 | 73.56 | 5.32 | 1759 | −0.8 | 9 | 16 | 20 | 10 | 10 | 1.330 | 650 | 75.8 | −33.7 | 49.6 |

condition, whereas the exiting plane of the mixing duct is set to the zeroth-order supersonic outflow condition.

### B. Freestream Conditions

In the Wilcox $k$-$\omega$ model [13], the turbulent kinetic energy is set to a small value in the freestream to prevent division by zero in the dissipation rate source term. However, in the present study, we specify $k = 0$ in the freestream and replace $k$ in the source term by $\tilde{k}$, defined in Eq. (1):

$$\tilde{k} = \max[k, \min(k_{\text{div}}, \tfrac{\omega\mu}{\rho})] \tag{1}$$

A user-specified constant that is generally set lower than one-tenth of the maximum value of $k$ throughout the boundary layer is $k_{\text{div}}$ [12]. This is verified numerically to not affect the laminar sublayer but to improve the robustness and efficiency of the integration significantly. The minimum between $k_{\text{div}}$ and $\omega\mu/\rho$ is taken, so that a clipping occurs only in nonturbulent flow regions in which an accurate representation of $\omega$ does not affect the accuracy of the flowfield. A value of $k_{\text{div}} = 1000\ \text{m}^2/\text{s}^2$ is used for all cases. The freestream $\omega$ is set to 10 $\text{m}^{-1}$ times the freestream velocity, as suggested by Wilcox [13].

### C. Global Performance Parameters

The mixing performance of the inlet can be quantified by global integrated parameters, such as fuel/air mixing efficiency. For the present study, the $\eta_m$ at the plane of interest (subscript $b$) is defined as the ratio of the local fuel mass flux that could react (if both temperature and pressure requirements are met) to the mass flux of the fuel provided by both cantilevered ramp injectors:

$$\eta_m = \int_b c_f^R \, \mathrm{d}\dot{m}/\dot{m}_f \tag{2}$$

$$c_f^R = \min[c_f, c_f^S \cdot (c_{\text{O}_2}/c_{\text{O}_2}^S)] \tag{3}$$

The mass flux of the reacting fuel ($c_f^R$) is defined in Eq. (3). The stoichiometric mass fraction of the fuels $c_{\text{CH}_4}^S$ and $c_{\text{C}_{12}\text{H}_{24}}^S$ are approximated as 0.0552 and 0.0638, whereas the corresponding stoichiometric mass fractions of the oxygen ($c_{\text{O}_2}^S$) for $CH_4$ and $C_{12}H_{24}$ are 0.2201 and 0.2182, respectively. It should be mentioned that the mixing efficiency in the present study only represents the degree of the bulk mixing. The effect of molecular mixing is not evaluated due to the limitation of the turbulence model. The flammability limits of the fuel are also not considered by this formulation.

The magnitude of the averaged stagnation pressure is often used to gauge the efficiency of the air-breathing engine component in experimental settings. However, stagnation pressure becomes an ineffective indicator when the variation in stagnation temperature is significant, which is the case with the fuel-injection inlet investigated

here. Thrust potential $\mathcal{F}_{\text{pot}}$, defined in Eq. (4), is used in the present study to estimate the thrust performance of the inlet. It calculates the momentum difference between the plane of interest and the flow in that plane reversibly expanded to a uniform back pressure at the nozzle exit area of the vehicle (subscript $c$) [17]. The turbulent kinetic energy $k$ is kept constant, and the flow is assumed to be chemically frozen, while the physical properties of the mixture are temperature-dependent:

$$\mathcal{F}_{\text{pot}} = -\mathcal{F}_{\text{pot,ref}} + \int_b \frac{\rho_c U_c^2 + P_c^\star}{\rho_c U_c} \, \mathrm{d}\dot{m}/\dot{m}_{\text{air,inlet}} \tag{4}$$

For the current study, the vehicle exit area is hypothetically chosen to be the same as the inlet-air captured area ($\mathcal{H}_{\text{inl}} \times \mathcal{W}_{\text{array}}$). The reference thrust potential is the oncoming airflow momentum at the initial cross section of the engine per unit mass of the airflow entering the engine. The initial thrust potential at the initial engine cross section is thus zero. The local mass flow rate $\dot{m}$ is determined numerically at each plane $b$, which ensures that it corresponds to the sum of the air and fuel flow rates. It should be mentioned that frictional, mixing, and shock losses can reduce the final thrust potential outcome.

### D. Grid Convergence Study

The WARP code has been extensively validated against available experimental data for similar high-speed flows in previous studies conducted by Alexander et al. [2], Parent et al. [18], and Sislian and Parent [19]. A grid convergence study is presented here to assess the accuracy of obtained results with the grid density employed. The computational grid for the present study is closely based on previous shcramjet studies [9,20]. The typical grid for the external compression region of the inlet consisted of $693 \times 223 \times 92 = 14.2$ million nodes, whereas the typical internal compression region of the inlet has $617 \times 201 \times 92 = 11.4$ million nodes. The three-dimensional open sectional grid views of both regions are illustrated in Fig. 3, where only every fifth node is shown.

Since the number of grid lines per unit distance is proportional to grid density, the inlets sharing the same grid density are expected to have similar grid-induced errors. The standard grid ($14.2 + 11.4 = 25.6$ million nodes) in the present study has a grid density factor $r$ of 1.00. The numerical simulation of case 8 is repeated and analyzed,

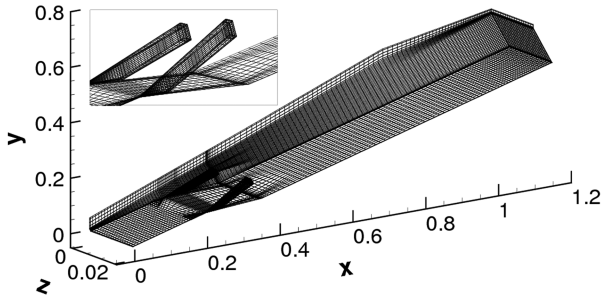


**a) External compression region**

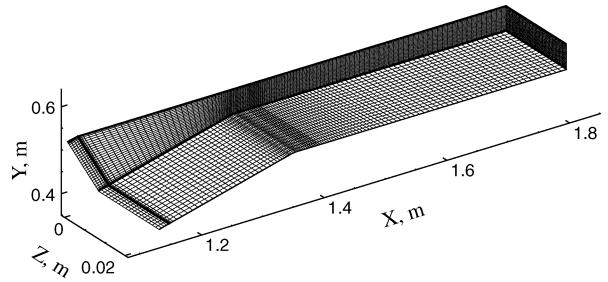


**b) Internal compression region**

**Fig. 3 Typical computational grid used (every fifth node is shown).**

**Table 5 Grid convergence factor**

| Case | Coarse | Standard | Fine |
|---|---|---|---|
| Grid density factor ($r$) | 0.66 | 1.00 | 1.50 |
| External compression region grid nodes | $4.32 \times 10^6$ | $14.2 \times 10^6$ | $47.5 \times 10^6$ |
| Internal compression region grid nodes | $3.57 \times 10^6$ | $11.4 \times 10^6$ | $36.4 \times 10^6$ |
| Total grid nodes | $7.89 \times 10^6$ | $25.6 \times 10^6$ | $83.9 \times 10^6$ |

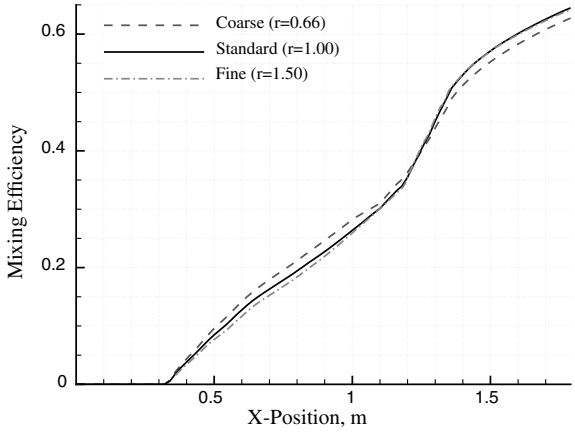


**a) Mixing efficiency**

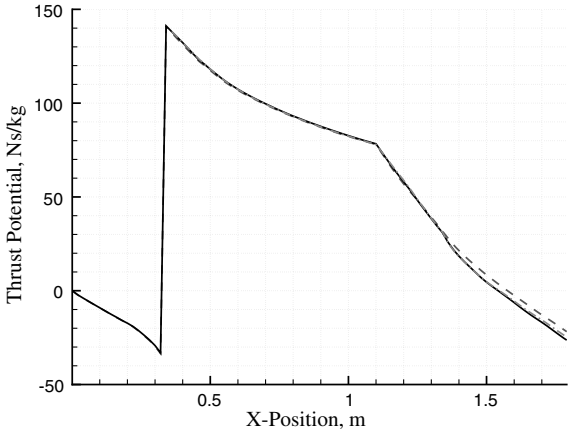


**b) Thrust potential**

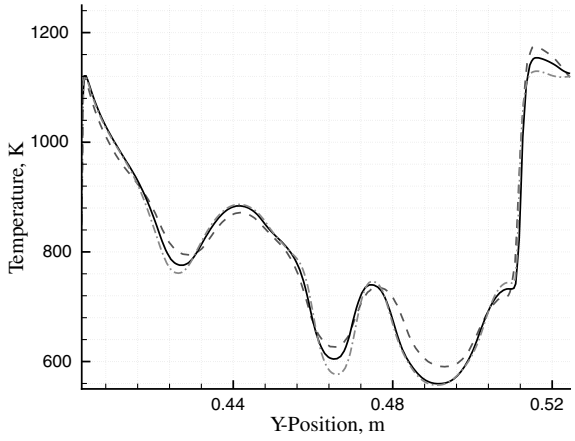


**c) Temperature along X=1.18m and Z=0.01m**

**Fig. 4 Grid convergence results.**

with grid densities of $r = 0.66$ and $r = 1.50$. Table 5 summarizes the numbers of nodes in each region with respect to $r$.

The global performance parameters and flowfields are observed to be very similar among the three cases, as seen in Fig. 4. Globally, the grid-induced error for the mixing efficiency is merely 2% between the coarse and fine grids at the $X = 1.8$ m plane. The standard grid only yields a 0.5% overestimate in $\eta_m$ when compared with the fine grid. The discrepancy in the prediction of thrust potential is slightly larger. Maximum errors of 10 and 6% are recorded in the $r = 0.66/r = 1.50$ and $r = 1.00/r = 1.50$ comparisons, respectively. Figure 4c shows the temperature variation in the $Y$ direction, with $X = 1.18$ m and $Z = 0.01$ m. The differences in temperature between the standard and fine grids are almost negligible. These small changes in both flow trends and properties are indicative of the small grid-induced errors for inlets with standard grid density. All inlet cases considered in the present paper employ a grid density factor of 1.00, and their grid-induced errors are expected to be minimal.

## IV. Results and Discussion

### A. General Flowfield Features

Characteristic features of the investigated fuel/air mixing flowfield configurations, as exemplified by case 2 in Table 1, are depicted in Fig. 5. Figure 5a represents cross-sectional variations of pressure and temperature at a lateral distance of $Z = 1.25$ mm, which is the center plane of the $\theta_{c1} = 9°$ injector. It can be seen that the inlet leading-edge shock is pushed upward by the strong bow shock generated by the cantilevered injector and merges with it (Fig. 6a). The shock formed under the cantilevered injector (wedge E in Figs. 2 and 5a) crosses the fuel/air interface boundary and intersects the upper shock at the cowl lip $C$. The second inlet shock formed at the cowl lip hits the shoulder $S$ of the inlet duct, creating a small recirculating region (Fig. 5b). The resulting reflected shock from this recirculation zone is seen to undergo a series of reflections from the internal duct walls, creating periodic high-pressure regions from $X = 1.32$ to $X = 1.8$ m.

The corresponding temperature fields in Figs. 5a and 5b show that the highest temperature occurs in the recirculation regions at $S$ and extends along the lower wall of the internal compression duct. The fuel/air equivalence ratio contours in that region, shown in Fig. 6b, reveal that no fuel is trapped inside the recirculation zone; therefore, premature ignition is unlikely to occur there.

The evolution of the fuel/air mixing process in the entire mixed-compression inlet, as characterized by the variations of its equivalence ratio, is depicted in Fig. 7. Shown are the strong vortices generated by the cantilevered ramp injectors that, after a slight downward displacement, are subsequently lifted off by the baroclinic torque effect after they cross the planar shock wave emanating from the wedge $E$ under the injectors at $X = 0.54$–$0.76$ m. Nevertheless, the combustible mixture reaches the wall at $X = 1.325$ m (Figs. 7i and 7j), where its equivalence ratio is of the order of $\phi = 0.23$ and well below the flammability limit of methane. Given the long ignition delay of methane, combustion is not likely to start immediately. At a distance of $X = 1.8$ m from the inlet leading edge (Fig. 7l), the mixture is still quite inhomogeneous with the equivalence ratio, ranging from $\phi \approx 1.0$ near the lower wall to $\phi \approx 0.1$ near the higher wall, with a maximum value of $\phi = 1.6$ in between. The overall mixing efficiency at the considered inlet exit section $X = 1.8$ is $\eta_m = 73.7\%$ (Table 1), for a global fuel/air equivalence ratio of $\phi = 1.06$.

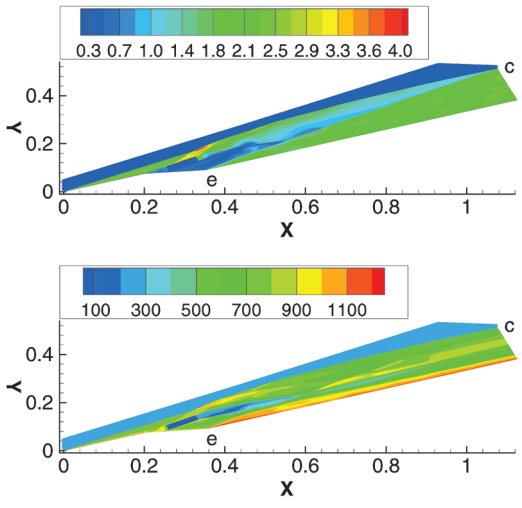


a) External compression region

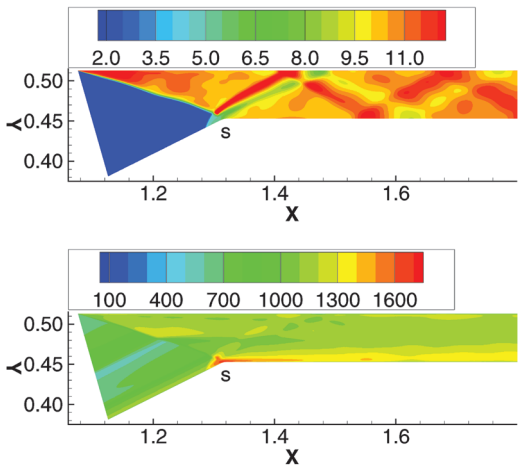


b) Internal compression region

**Fig. 5 Pressure and temperature contours in the inlet at $Z = 1.25$ mm plane, case 2.**

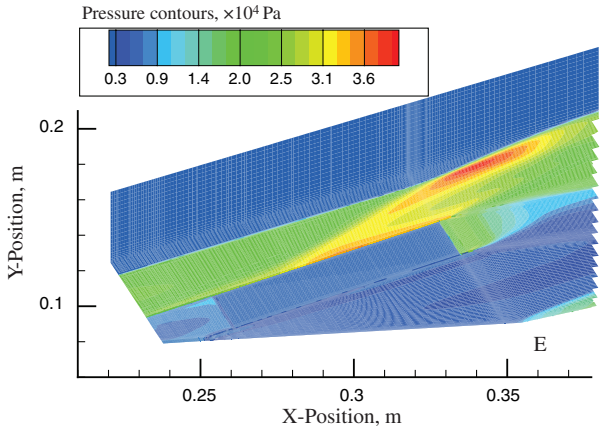


a) Pressure contours near fuel injectors

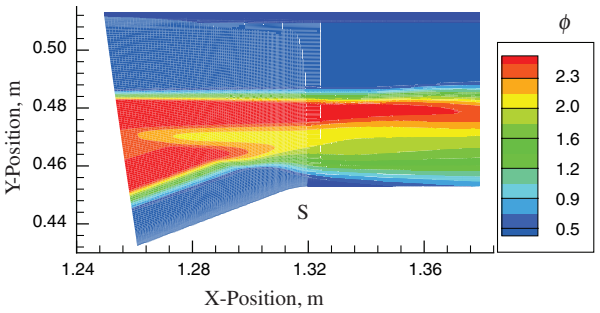


b) Equivalence ratio contours near shoulder

**Fig. 6 Contours at the $Z = 1.25$ mm plane, case 2.**

### B. Effect of Inlet Compression and Stagnation Temperature of Injected Fuel

The impact of the degree of compression on $\eta_m$ and $\mathcal{F}_{\text{pot}}$ of the employed two-shock inlet is assessed by setting its leading-edge angle to $\theta_{\text{inl}} = 16.4$ and $20.7°$, which correspond to inlet pressure ratios of $\approx$46 and $\approx$75 and area ratios ($\mathcal{H}_{\text{inl}}/\mathcal{H}_{\text{duct}}$) of about $\approx$7.4 and $\approx$8.5, respectively, as summarized in Tables 1 and 2. The exit pressure $P_f$ of the injected gaseous methane is matched to that of its surrounding airflow, and the fuel-injected temperature $T_f$ is chosen to be in between its boiling and self-ignition values. The targeted fuel/air equivalence ratios $\phi$ are reached by choosing the appropriate magnitude of the fuel exit velocity $U_{\text{fuel}}$. The actual values of $\phi$, as well as the inlet dimensions, are determined interactively via numerical simulation. The resulting average inlet exit flow variables, fuel-injection parameters, $\phi$, $\eta_m$, and $\mathcal{F}_{\text{pot}}$ are presented in Tables 1 and 2. The axial evolution of $\eta_m$ and $\mathcal{F}_{\text{pot}}$ for all considered cases are shown in Figs. 8 and 9.

Figure 8 clearly demonstrates the impact of the inlet compression on the overall mixing efficiency and thrust potential. The inlet compression is seen to have the strongest impact on $\eta_m$, since case 2 and case 4 outperform case 1 and case 3 by 16.4 and 19.3%, respectively. The stagnation temperature of the injected fuel $T_f^\circ$, which controls $U_f$ and $\dot{m}_f$, is found to affect $\eta_m$ as well. Raising $T_f^\circ$ from 800 to 1400 K can boost mixing efficiency by 13.2%, as illustrated in Fig. 9: cases 3 $\rightarrow$ 1 and 7 $\rightarrow$ 8. It can also be observed that there is a direct correlation between $T_f^\circ$ and the inlet dimensions $\mathcal{L}_{\text{cowl}}$ and $\mathcal{H}_{\text{inl}}$ due to an increase in $\dot{m}_f$, leading to an increase in the inlet leading-edge shock strength. Consequently, longer $\mathcal{L}_{\text{cowl}}$ and taller $\mathcal{H}_{\text{inl}}$ become necessary for the leading-edge shock and the shock emanating from underneath the cantilevered ramp injector to merge at the cowl lip. Interestingly, the inlet internal compression duct height $\mathcal{H}_{\text{duct}}$ remains almost constant for all the cases considered, regardless of the fuel-injection properties and changes in the inlet dimensions.

The corresponding variations of the thrust potential that reflect losses incurred in the inlet flowfield, including losses due to mixing, are also shown in Figs. 8 and 9. After an initial drop of $0 \rightarrow I$, which reflects the losses generated by the cantilevered ramp injector system, the thrust potential increases sharply at the exit plane of injectors $I$ due to the momentum of the quasi-parallel fuel injection. Thereafter, $I \rightarrow C$, the thrust potential gradually decreases mainly due to mixing losses. The rate of decrease of the thrust potential increases at $C$, where the second reflected shock is generated. It can be seen that case 1, with $T_f^\circ = 1400$ K and $\theta_{\text{inl}} = 20.7°$, attains the highest thrust potential $\mathcal{F}_{\text{pot}} = -2.5$ Ns/kg with an attendant $\eta_m = 63.5\%$. This can be compared with case 4, which exhibits much lower thrust potential $\mathcal{F}_{\text{pot}} = -107.9$ Ns/kg and slightly higher mixing efficiency $\eta_m = 68.8\%$ with $\theta_{\text{inl}} = 20.7°$ and $T_f^\circ = 800$ K. In case 6, a three-shock mixed-compression inlet, illustrated in Fig. 1, with the first two shocks having equal strengths, is considered in an attempt at

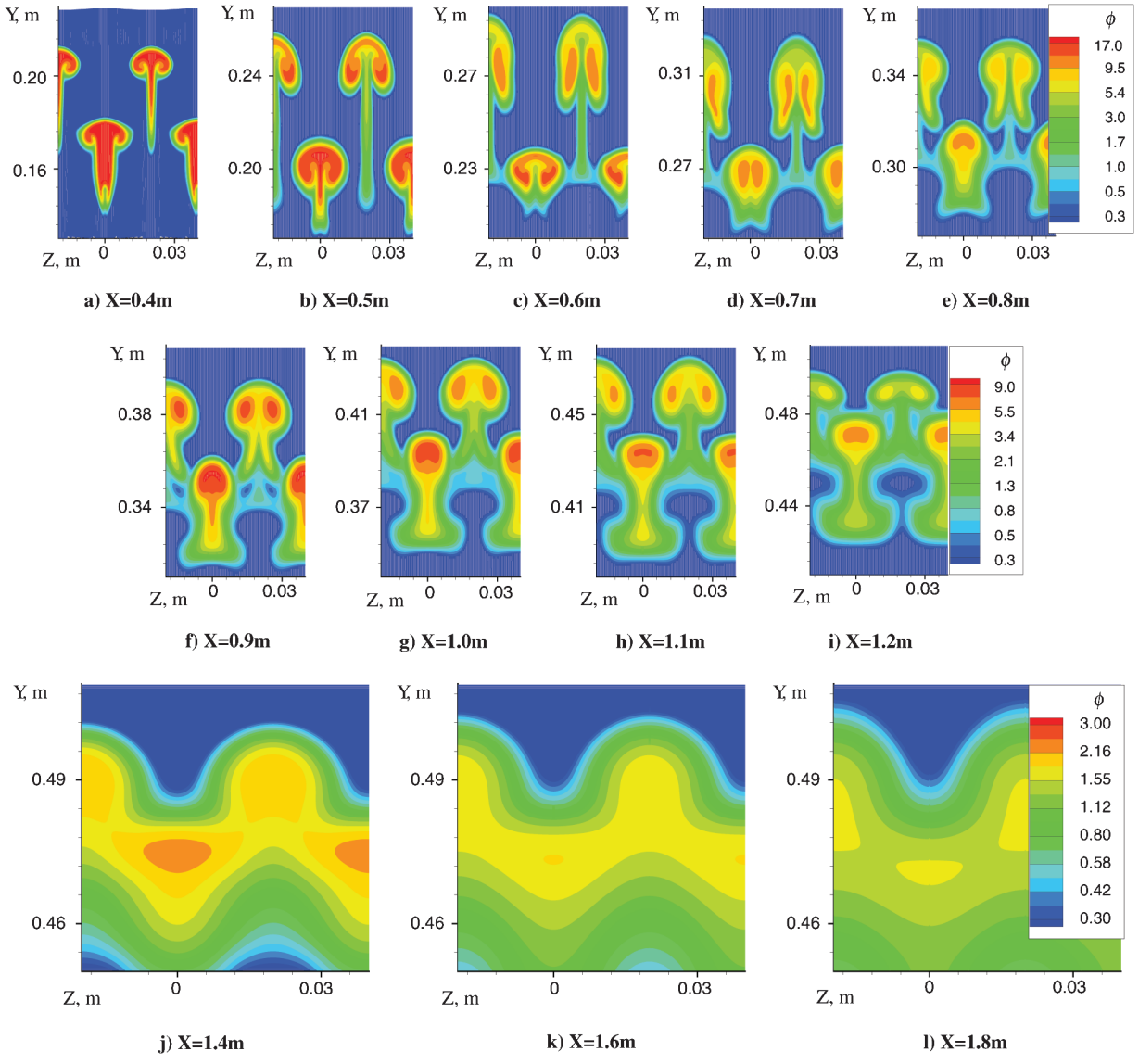


**Fig. 7 Equivalence ratio contours at selected axial locations, case 2.**

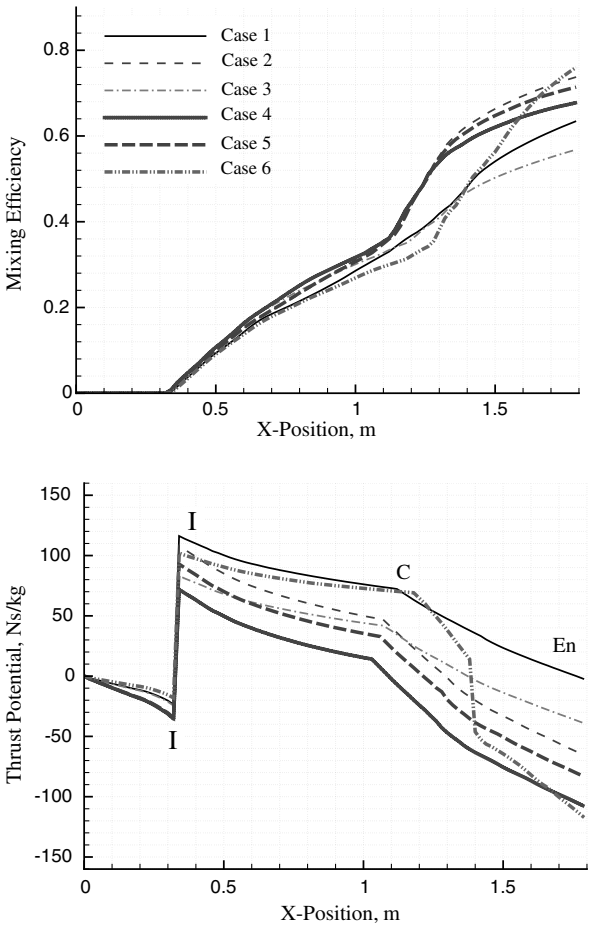


**Fig. 8 Effect of inlet compression $\theta_{\text{inl}}$.**

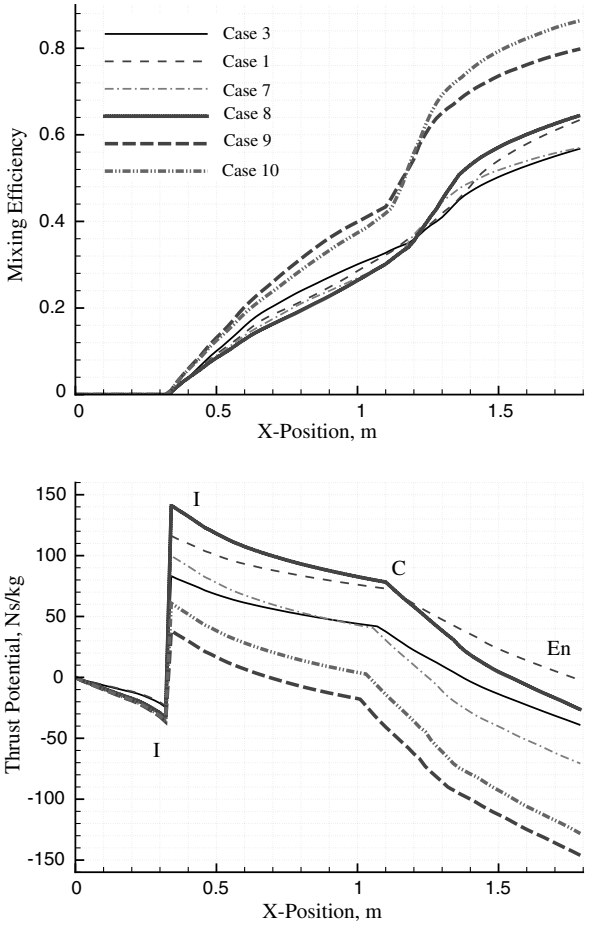


**Fig. 9 Effect of stagnation temperature of injected fuel $T_f^\circ$.**

increasing the compression ratio. The resulting pressure and equivalence ratio contours are presented in Fig. 10. An air slot injection, located at 20 mm upstream of the first inlet shoulder $S$, is necessary to eliminate the substantial recirculation region formed by the shock-boundary layer at $S$. It is seen in Fig. 8, $X \approx 1.4$ m, that the injection slot causes a sharp drop in the thrust potential. A slight increase in mixing efficiency when compared with case 4, at the same axial distance of $X = 1.8$ m, has been achieved for a relative 30% increase in the compression ratio. Moreover, the fuel/air mixture reaches the lower wall boundary layer immediately after the third shock (Fig. 10).

### C. Effect of Fuel Molecular Weight and Fuel/Air Equivalence Ratio

A relatively heavy hydrocarbon fuel (gaseous kerosene), represented by $C_{12}H_{24}$, is considered in order to quantitatively evaluate the effect of fuel molecular weight on the mixing performance of fuel injection in the inlet and the losses incurred on the resulting thrust potential. Kerosene fuel is widely used in aerospace propulsion systems due to its good ignition characteristics (as compared with methane), high heating value, and advantages in onboard fuel storage system. However, as a result of its higher reactivity, its compression ratio in the inlet must be lower to avoid premature ignition, as indicated in Table 3 (cases 11 and 12). Nevertheless, for the sole purpose of comparison, a $\theta_{\text{inl}} = 20.7^\circ$ kerosene inlet (case 14), which has identical $T_f^\circ$ and $\phi$ as the $\theta_{\text{inl}} = 20.7^\circ$ methane inlet (case 4), is chosen to assess the effect of fuel molecular weight. The constraints imposed on the fuel-injection properties, $P_f$, $T_f$, $U_f$, and $T_f^\circ$ are obeyed. From Table 3 (cases 4 and 14), it is demonstrated that the mixing efficiency for kerosene is only 6.5% lower than that of methane, even though its molecular weight is more than tenfold heavier. It can safely be concluded that the molecular weight of hydrocarbon fuels do not particularly affect the mixing process.

As expected, for both methane and kerosene cases, the mixing efficiency increases with the decrease of global equivalence ratio, which also negatively affects the thrust performance of the inlets. Comparing case 11 with 12 and case 10 with 13, it is evident that, for a comparable decrease in the equivalence ratio $\phi$, the gain in $\eta_m$ for kerosene is near 23%, which is much higher than that of methane

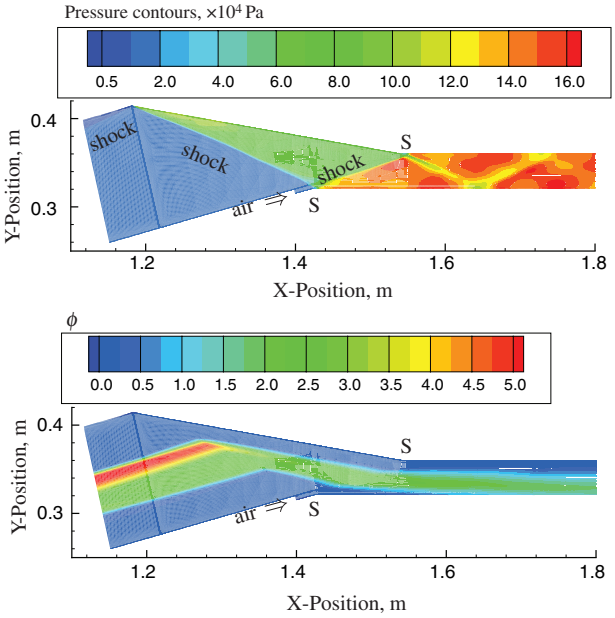


**Fig. 10 Contours in the three-shock inlet at $Z = 18.75$ mm plane, case 6.**

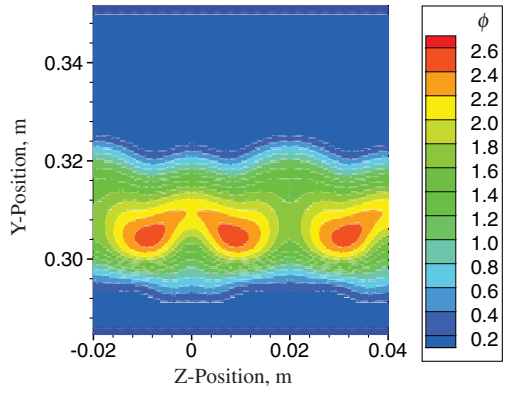


**a) X=1.367m**

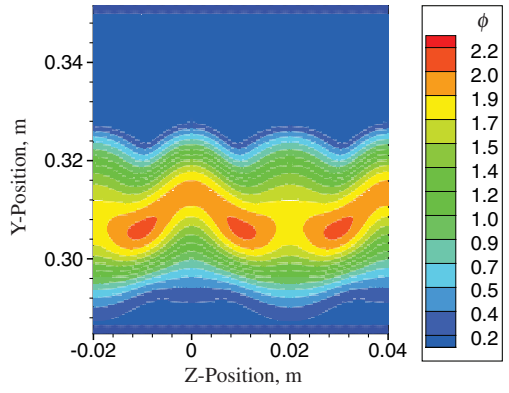


**b) X=1.5m**

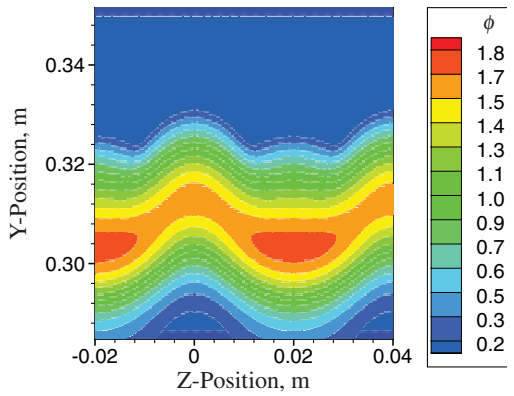


**c) X=1.8m**

**Fig. 11 Equivalence ratio contours at selected axial locations, case 12.**

(about 10.8%). The corresponding decreases in thrust potential $\mathcal{F}_{\text{pot}}$ are 41.1 and 20%, respectively. Figures 11 and 12 depict the mixing evolution along $X$ for both fuel-lean cases. Those equivalence ratio contours reveal that the bulk of combustible kerosene/air mixture never reaches the walls of the inlet internal compression duct within the computational domain (1.8 m), whereas the methane/air mixture reaches the lower duct wall at $X \approx 1.235$ m, which is about 5 mm downstream of the inlet shoulder $S$. At this section, the equivalence ratio is $\phi \approx 0.25$, which is well below its flammability limit of 0.46, the temperature is of the order of 1850 K, and the mixing efficiency is $\eta_m = 80\%$.

### D. Premature Ignition

For the concept of fuel injection in the inlet of a scramjet engine to be viable, it is imperative that premature ignition of the combustible mixture before the engine combustor be avoided. Close examination of flowfields in all cases reported in Tables 1–4 revealed that, except for case 18, fuel does not interact with the boundary layer in the external compression region of the inlet nor in the internal compression duct before the recirculation zone. Results of numerical simulations also show that, within the internal compression duct, combustible kerosene/air mixtures (cases 11 and 12) remain away from the duct walls, whereas all methane mixtures penetrate the boundary layer of the lower wall, where its thickness is at the order of 10–12 mm, and the maximum temperature reaches as high as 1750 K at equivalence ratios of $\phi \approx 0.25$. However, given the long ignition delay times of methane and its short residence time in the compression duct, combustion is not likely to start immediately. Nevertheless, to confirm the absence of premature ignition and combustion, a chemically reacting situation of case 8, which is typical of all the methane cases considered in Tables 1–4, is evaluated by using a finite-rate methane/air chemical reaction mechanism, proposed by Yungster and Rabinowitz [21], that contains 52 elementary reactions and 20 species. Results indicate that the only

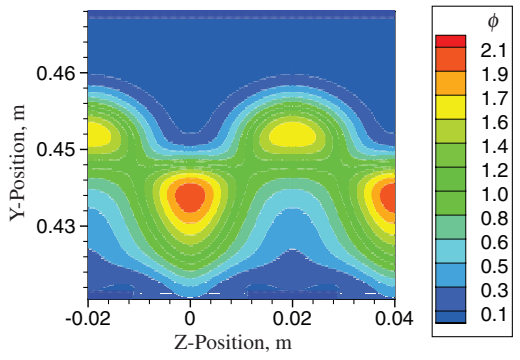


**a) X=1.235m**

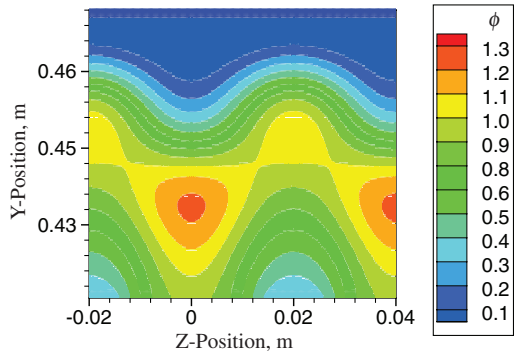


**b) X=1.5m**

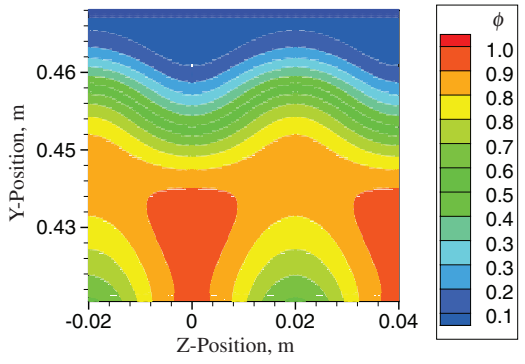


**c) X=1.8m**

**Fig. 12 Equivalence ratio contours at selected axial locations, case 13.**

difference from the corresponding nonreacting case is the presence of minute amounts of $CH_3$ (mass fraction in the order of $10^{-7}$) within the internal compression duct boundary layers.

### E. Effect of Injector Geometry

As mentioned above, the adopted baseline injector configuration in the present study, as illustrated in Fig. 2, has been shown to exhibit high mixing efficiency with minimal losses for gaseous hydrogen injection at Mach 11 [1]. To assess its supersonic mixing performance in the present case of heavier hydrocarbon fuel injection into an inlet at a flight Mach number of 8, a limited parametric study is performed by keeping $\theta_{\text{inl}}$ and methane fuel-injection parameters $P_f^\circ$, $T_f^\circ$, and $T_f$ constant and varying solely the geometric parameters $\theta_s$, $\theta_{c1}$, $\theta_{c2}$, $\mathcal{W}_{\text{array}}$, $\mathcal{H}_{\text{inj}}$, and $\mathcal{W}_{\text{inj}}$ of the injector (Table 4). Only one parameter, shown in Fig. 2, is modified, with all other parameters kept constant.

Results reported in Table 4 indicate that injector geometry has a strong influence on the inlet dimensions. A slight 0.8° change in the injector sidewall negative sweep angle can result in a 9.1% increase in the inlet height $\mathcal{H}_{\text{inl}}$, 9.8% in the internal compression duct height $\mathcal{H}_{\text{duct}}$, and 8.2% in the inlet external compression length $\mathcal{L}_{\text{cowl}}$. Global performance parameters for all cases considered in Table 4 show that the baseline injector, case 8, outperforms all other cases by 6.8–29.5% in mixing efficiency. It can be reasonably assumed that the baseline injector geometry also exhibits superior performance when hydrocarbon fuels are preinjected into the inlet of a Mach 8 engine. It should be noted that case 17 has the highest thrust potential and lowest mixing efficiency because reduced injector array spacing increases the equivalence ratio $\phi$ by 22.7% when compared with case 8.

## V. Conclusions

The feasibility of hydrocarbon fuel injection into the mixed-compression inlet for the flight Mach number of 8 is numerically verified in the present study. The implementation of cantilevered ramp fuel injectors and equal-angle shocks are proved to be successful in minimizing interactions between the combustible fuel/air mixture and the high-temperature boundary layers. It is demonstrated that the mixing efficiencies in the range of 75.5–95.8% can be achieved for the methane-fueled inlet with a low risk of premature ignition.

The parametric study reveals that both inlet compression ratio and fuel-tank stagnation temperature have strong influences on the global performance parameters. Increasing the inlet wedge angle from 16.4 to 20.7° can result in a 16.4–19.3% improvement in the mixing efficiency and a decline of 62.9–68.8 Ns/kg in the thrust potential. Similarly, raising the fuel-tank stagnation temperature from 800 to 1400 K can increase the mixing efficiency by 11.8–13.2%. The injector parametric study confirms the applicability of the previously optimized Mach 11 hydrogen injector to the current Mach 8 methane inlets. The positive impacts of increasing the sweep angle and employing alternating compression angles reported in the present study are in agreement with previous claims.

The impact of the fuel molecular weight is assessed through a comparison of the performance of methane- and kerosene-fueled inlets. It is found that using a lighter fuel can enhance the degree of mixing. Methane is shown to provide the best mixing efficiency, mainly due to its ability to withstand high-compression ratio and fuel-tank stagnation temperature conditions and its low molecular weight. The mixing efficiencies of methane and kerosene are also shown to be comparable, despite the difference in their molecular weights.

## Acknowledgment

This work is sponsored by Defence Research and Development Canada, Valcartier, Quebec. Their financial support is gratefully acknowledged.

## References

[1] Sislian, J. P., and Parent, B., "Hypervelocity Fuel/Air Mixing in a Shcramjet Inlet," *Journal of Propulsion and Power*, Vol. 20, No. 2, 2004, pp. 263–272. doi:10.2514/1.9252

[2] Alexander, D. C., Sislian, J. P., and Parent, B., "Hypervelocity Fuel/Air Mixing in Mixed-Compression Inlets of Shcramjets," *AIAA Journal*, Vol. 44, No. 10, 2006, pp. 2145–2155. doi:10.2514/1.12630

[3] Vinogradov, V. A., Shikhman, Y. M., and Segal, C., "Review of Fuel Pre-Injection Studies in a High Speed Airflow," AIAA 44th Aerospace Sciences Meeting and Exhibit, AIAA Paper 2006-1030, Jan. 2006.

[4] Vinogradov, V. A., and Prudnikov, A. G., "Injection of Liquid Into the Strut Shadow At Supersonic Velocities," SAE Aerospace Atlantic Conference and Exposition, Society of Automotive Engineers Paper SAE-931455, Troy, MI, April 1993.

[5] Livingston, T., Segal, C., Schindler, M., and Vinogradov, V. A., "Penetration and Spreading of Liquid Jets in an External-Internal Compression Inlet," *AIAA Journal*, Vol. 38, No. 6, 2000, pp. 989–994. doi:10.2514/2.1082

[6] Owens, M., Mullagiri, S., Segal, C., and Vinogradov, V. A., "Effects of Fuel Preinjection on Mixing in Mach 1.6 Airflow," *Journal of Propulsion and Power*, Vol. 17, No. 3, 2001, pp. 605–610. doi:10.2514/2.5784

[7] Vinogradov, V. A., Shikhman, Y. M., Albegov, R. V., and Vedeshkin, G. K., "Experimental Research of Pre-Injected Methane Combustion in High-Speed Subsonic Airflow," AIAA 12th International Space Planes and Hypersonics Systems and Technologies Conference, AIAA Paper 2003-6940, Dec. 2003.

[8] Guoskov, O. V., Kopchenov, V. I., Lomkov, K. E., Vinogradov, V. A., and Walrup, P. J., "Numerical Research of Gaseous Fuel Preinjection in Hypersonic Three-Dimensional Inlet," *Journal of Propulsion and Power*, Vol. 17, No. 6, 2001, pp. 1162–1169. doi:10.2514/2.5890

[9] Sislian, J. P., Martens, R. J., Schwartzentruber, T. E., and Parent, B., "Numerical Simulation of a Real Shcramjet Flowfield," *Journal of Propulsion and Power*, Vol. 22, No. 5, 2006, pp. 1036–1048. doi:10.2514/1.14895

[10] Alexander, D. C., and Sislian, J. P., "Computational Study of the Propulsive Characteristics of a Shcramjet Engine," *Journal of Propulsion and Power*, Vol. 24, No. 1, 2008, pp. 34–44. doi:10.2514/1.29951

[11] Parent, B., "Computational Study of Fuel Injection in a Shcramjet Inlet," Ph.D. Thesis, Graduate Dept. of Aerospace Science and Engineering, Univ. of Toronto, Toronto, ON, Canada, 2002.

[12] Parent, B., and Sislian, J. P., "The Use of Domain Decomposition in Accelerating the Convergence of Quasihyperbolic Systems," *Journal of Computational Physics*, Vol. 179, No. 1, 2002, pp. 140–169. doi:10.1006/jcph.2002.7048

[13] Wilcox, D. C., "Reassessment of the Scale Determining Equation for Advanced Turbulence Model," *AIAA Journal*, Vol. 26, No. 11, 1988, pp. 1299–1310. doi:10.2514/3.10041

[14] Roe, P. L., "Approximate Riemann Solvers, Parameter Vectors, and Difference Schemes," *Journal of Computational Physics*, Vol. 43, No. 2, 1981, pp. 357–372. doi:10.1016/0021-9991(81)90128-5

[15] Yee, H. C., Klopfer, G. H., and Montagné, J.-L., "High-Resolution Shock-Capturing Schemes for Inviscid and Viscous Hypersonic Flows," *Journal of Computational Physics*, Vol. 88, No. 1, 1990, pp. 31–61. doi:10.1016/0021-9991(90)90241-R

[16] Beam, R. M., and Warming, R. F., "An Implicit Factored Scheme for the Compressible Navier–Stokes Equations," *AIAA Journal*, Vol. 16, No. 4, 1978, pp. 393–402. doi:10.2514/3.60901

[17] Parent, B., and Sislian, J. P., "Effect of Geometrical Parameters on the Mixing Performance of Cantilevered Ramp Injectors," *AIAA Journal*, Vol. 41, No. 3, 2003, pp. 448–456. doi:10.2514/2.1966

[18] Parent, B., Sislian, J. P., and Schumacher, J., "Numerical Investigation of the Turbulent Mixing Performance of a Cantilevered Ramp Injector," *AIAA Journal*, Vol. 40, No. 8, 2002, pp. 1559–1566. doi:10.2514/2.1824

[19] Sislian, J. P., and Parent, B., "Validation of Wilcox *k-w* Model for Flows Characteristic to Hypersonic Airbreathing Propulsion," *AIAA Journal*, Vol. 42, No. 2, 2004, pp. 261–270.

doi:10.2514/1.1989
[20] Schwartzentruber, T. E., Sislian, J., and Parent, B., "Suppression of Premature Ignition in the Premixed Inlet Flow of a Shcramjet," *Journal of Propulsion and Power*, Vol. 21, No. 1, 2005, pp. 87–94. doi:10.2514/1.7003
[21] Yungster, S., and Rabinowitz, M. J., "Computation of Shock-Induced Combustion Using a Detailed Methane-Air Mechanism," *Journal of Propulsion and Power*, Vol. 10, No. 5, 1994, pp. 609–627. doi:10.2514/3.23770

C. Segal
*Associate Editor*